Catalysis Science & Technology

Accepted Manuscript

This article can be cited before page numbers have been issued, to do this please use: K. Christoforidis and M. Fernandez Garcia, *Catal. Sci. Technol.*, 2015, DOI: 10.1039/C5CY00929D.

ROYAL SOCIETY OF CHEMISTRY

www.rsc.org/catalysis

View Article Online
DOI: 10.1039/C5CY00929D

Catalysis Science & Technology

ARTICLE

Photoactivity and charge trapping sites in Copper and Vanadium doped TiO_2 anatase nano-materials

Received 00th January 20xx,
Accepted 00th January 20xx

DOI: 10.1039/x0xx00000x

www.rsc.org/

Konstantinos C. Christoforidis[a,b,*] and Marcos Fernández-García[a]

Two series of Cu^{2+} and V^{4+} doped TiO_2 anatase samples were prepared using the microemulsion synthetic route by varying the metal/Ti ratio. The samples were characterized by UV-Vis absorption, nitrogen physisorption, XRD, Raman, XPS and EPR spectroscopy. Their photocatalytic activity against toluene photo-oxidation was evaluated under both sunlight-type and pure UV light irradiation. The photoactivity was drastically affected by the dopant content. Low or moderate metal doping was beneficial for toluene photo-degradation, while high doping levels suppressed photoactivity. Electron paramagnetic resonance (EPR) spectroscopy was employed to study the structure and electronic characteristics of the prepared catalysts and to elucidate the physicochemical aspects governing photoactivity. The presence of different Cu- and V-species was detected as a function of the metal content in the catalyst. EPR spectroscopy revealed that photoinitiated charge formation takes place in both Cu and V doped TiO_2 series and that charge separation may be enhanced depending on the dopant content. A direct correlation between the dopant species formed and the holes-formation was observed in both series. Photoactivity is directly correlated with the formation of holes, which in turn is tuned by the dopant content regulating the isolated metal centers versus metal clusters formation. Low or moderate doping levels enhanced the separation of photo-produced electron-hole pairs via accepting e^-, eliminating trapping sites related to localized Ti^{3+} states and increasing the abundance of hole species. At higher levels where metal clusters prevailed, dopants acted as recombination centers deteriorating photoactivity in both TiO_2-doped series. The results indicate a general mechanism potentially applicable in similar photocatalytic systems.

1. Introduction

Photocatalysis using semiconductor nanomaterials is an attractive method for environmental protection and energy conversion since it can be applied at ambient conditions (room temperature and atmospheric pressure) using solar energy as the energy source.[1,2] Among the different photocatalysts presented in the literature, nanostructured titanium dioxide (TiO_2) is definitely the most frequently employed due to its inherent properties (non-toxic, low cost, high stability).[1,2] Many attempts have been made to improve and optimize the properties of TiO_2 towards realistic application of heterogeneous photocatalysis. Much efforts have been devoted on narrowing the relatively wide band gap of TiO_2 (~ 3.2 eV for anatase) targeting on its activation by visible light. Towards this objective, doping with transition metals has been largely employed to decrease the band gap energy or to introduce energy levels inside the band gap.[1,3,4]

Since the photocatalytic efficiency of titania in organic degradation reactions is usually defined by the available photogenerated charges,[2,5,6] efforts have been devoted on extending the life time of such centers either through the synthesis of multi-phase materials, composites or metal-doped TiO_2.[7-17] In the case of doping, in addition to the desired red-shift of the adsorption spectrum and in some cases the reported efficient separation of the photogenerated charges, the presence of transition metals has also been related with potential negative impacts such as acting as recombination centers or introducing defective sites in the crystal lattice and increasing the probability of electron/hole (e^-/h^+) recombination.[1,3,18-20] Studies have been performed on charge trapping and recombination[21,22] as well as on understanding the factors affecting such processes.[23,24] Nevertheless, conflicting results have been presented in the literature regarding TiO_2 doped with transition metals. This is related to the complex physicochemical effects originating from the doping process which show dependence of a significant number of structural/electronic variables, which in turn originate already from the preparation method and would ultimately control the performance of the photocatalyst.

Copper and vanadium are among the most used transition metals as TiO_2 dopants[25-30] since they can lead to significant absorption in the visible region of light. TiO_2 nanomaterials loaded with Cu or V have been developed and studied in a variety of photo-initiated reactions[30-36] presenting either

[a] Instituto de Catálisis y Petroleoquímica, CSIC, C/Marie Curie 2, 28049-Madrid, Spain.
[b] Department of Chemical and Pharmaceutical Sciences, University of Trieste, 34127 Trieste, Italy.
* e-mail: kchristoforidis@units.it

Electronic Supplementary Information (ESI) available: Photoreactor details, time-on-stream evolution of the photocatalytic efficiency, surface atomic ratio.

View Article Online
DOI: 10.1039/C5CY00929D

increased or decreased photoactivity. Mechanistic schemes including the introduction of new energy levels in the band gap of TiO_2 and the participation in the charge transfer processes such as trapping of photogenerated electrons and holes and O_2 reduction have been proposed.[31,36,37] Gray and co-workers studied the copper loading effect on the electron paramagnetic resonance (EPR) characteristics of surface modified rutile TiO_2.[38] Mixed phase anatase/rutile nanomaterials doped with vanadium presented high activity under visible light irradiation.[39] Co-doped materials have been also studied where copper and vanadium proposed to act as electron scavenger facilitating charge separation.[36,40] However, despite the great interest and the numerous studies in the literature in transition metal doped TiO_2, very few works report a systematic study and detailed combined analysis of the dopants' species present, the photogenerated charge carriers, the direct observation of their trapping sites in the final nanomaterial and their effect in photoactivity. Particularly for the case of Cu^{2+} and V^{4+} in anatase-based nanomaterials, such study has never been reported to the best of our knowledge.

The present work outlines the preparation of two series of doped anatase titania using Cu^{2+} and V^{4+} prepared by chemically interaction with species coming from the titanium isopropoxide precursor using the microemulsion procedure in an effort to minimize the differences between the samples prepared. Materials with primary particle size and textural properties in a comparable range were developed. The catalysts were evaluated against sunlight and UV-light gas-phase photo-oxidation of toluene and EPR spectroscopy was applied to study both the structure as well as the photogenerated charges in the nanomaterials. Electron and hole pairs generated by light irradiation and trapped in TiO_2 were investigated in order to relate their abundance and stability with the catalytic activity and the catalyst's composition linked with the dopants species. The relationship between the structure, the dopants species, the photogenerated charges and the catalytic activity is discussed on the basis of the combined catalytic and spectroscopic study. The two series prepared using different and widely applied transition metals as TiO_2 dopants were studied in an effort to validate the consistency of the mechanism proposed herein.

2. Materials and Methods

2.1 Catalyst preparation

Titania precursor materials were prepared using a microemulsion synthetic route by addition of titanium(IV) isopropoxide (Aldrich) to an inverse emulsion containing an aqueous phase (50 ml) dispersed in n-heptane (85/10 v/v vs. H_2O; Panreac), and using Triton X-100 (variable quantity; Aldrich) as surfactant, in 1-hexanol (105/100 v/v vs. surfactant; Aldrich). The metal (Cu^{2+} or V^{4+}) was introduced from copper nitrate and vanadyl acetylacetonate (Aldrich). The final atomic content of the metal (x %) varied from 0.05 to 1 % (stoichiometry: $Ti_{1-0.0x}M_{0.0x}O_y$). The resulting mixture was vigorously stirred for 24 h, centrifuged, decanted, thoroughly rinsed under stirring with methanol in order to eliminate any portion from the organic and surfactant media, and dried at 110 ^oC for 24 h. The dried precipitates were calcined in air at 500 ^oC for 2h using a ramp of 1 $^oC\ min^{-1}$. A reference material was also synthesized using the same procedure without the presence of the doped metal. Sample labels are: T for pure TiO_2, TCu*x* and TV*x* for Cu- and V-doped TiO_2 respectively (where *x* corresponding to the atomic percentage of the metal).

2.2 Characterization techniques

Brunauer, Emmett and Teller (BET) surface area and porosity measurements were carried out by N_2 adsorption at 77K using a Micromeritics 2010 instrument. The nitrogen adsorption volume at the relative pressure (P/P_0) of 0.98 was used to determine the pore volume and average pore diameter. XRD patterns were recorded in the range $10^o < 2\vartheta < 120^o$ using 0.02^o steps, using a Siemens D-501 diffractometer with Ni filter and graphite monochromator with a Cu K_α X-ray source. UV-visible diffuse reflectance spectroscopy experiments were performed with a Shimadzu UV2100 apparatus with a nominal resolution of ca. 1 nm using $BaSO_4$ as reference. Band gap analysis was done following standard procedures by plotting $(h\nu\alpha)^{1/2}$ ($h\nu$ = excitation energy, α = absorption coefficient) vs. energy.[18] Raman spectra were recorded using a Horiba iH320 spectrometer and He:Ne laser excitation (632.8 nm).

XPS data were recorded on 4 × 4 mm^2 pellets, 0.5 mm thick, prepared by slightly pressing the powder materials which were outgassed in the prechamber of the instrument at room temperature up to a pressure < 2×10^{-8} Torr to remove chemisorbed water from their surfaces. The SPECS spectrometer main chamber, working at a pressure <10^{-9} Torr, was equipped with a PHOIBOS 150 multichannel hemispherical electron analyser equipped with a dual X-ray source working with Al K_α ($h\nu$ = 1486.2 eV). The C 1s peak at 284.6 eV was used to correct charging effects.

EPR measurements were carried out with a Bruker ER200D instrument operating in the X-band. All spectra were recorded at 77 K in a double T type cavity. The frequency of the microwave was calibrated using diphenyl-picryl-hydrazyl (DPPH) as standard (with g = 2.0036) located in the second cavity. For outguessing treatments, 60 mg of the Ti-sample were placed in a quartz cell and vacuum treated at pressures down to 2×10^{-5} Torr at room temperature for 1 h. Irradiation treatments were carried out at liquid nitrogen temperature (77 K), by placing the EPR cell in a quartz Dewar flask, unless otherwise stated. The samples were irradiated with UV-light for specific periods using four lamps (Philips TL 6W/08, identical to those used in the catalytic experiments) symmetrically positioned outside of the sample. EPR spectra were simulated using EasySpin software package.[41]

2.3 Photo-catalytic experimental details

Activity for the gas-phase photo-oxidation of toluene was tested in a continuous flow annular photoreactor (see Figure S1 at Electronic Supplementary Information)[42] containing ca.

View Article Online
DOI: 10.1039/C5CY00929D
Catal. Sci. Technol. Article

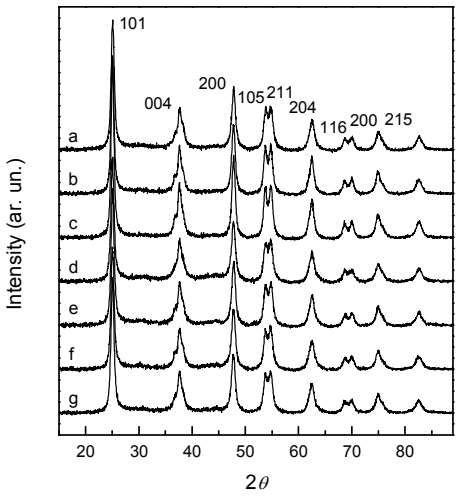

Figure 1. XRD patterns of the pure TiO_2 (a), the TCu*x* (TCu005 (b), TCu01 (c), TCu1 (d)) and the TV*x* nanomaterial (TV005 (e), TV01 (f) and TV1 (g)).

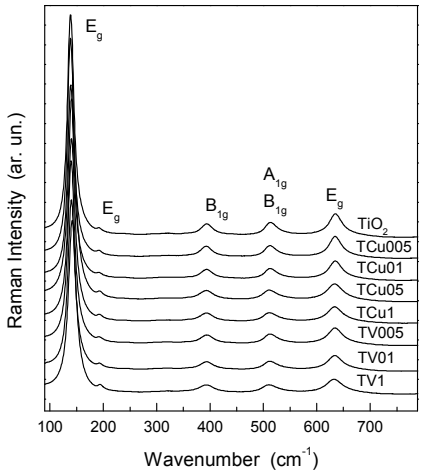

Figure 2. Raman spectra of the indicated pure (T) and metal doped (TCu*x* and TV*x*) samples.

40 mg of photocatalyst as a thin layer coating on a pyrex tube, corresponding to TiO_2 surface density of 0.5 mg/cm^2. The corresponding amount of catalyst was suspended in 1 ml of water, painted on a pyrex tube (cut-off at ca. 290 nm) and dried at room temperature. The reacting mixture (100 ml/min) was prepared by injecting toluene (Panreac, spectroscopic grade) into a wet (ca. 75% relative humidity) 20 vol.% O_2/N_2 flow before entering at room temperature to the photoreactor, yielding an organic inlet concentration of ca. 800 ppmv (velocity 1.33 cm/s). After flowing the mixture for 3-4 h in the dark (control test), the catalyst was irradiated by four lamps symmetrically positioned outside the photoreactor. The photocatalytic tests were performed under a radiation spectrum simulating sunlight (Philips TL 6W/54-765; Color rendering index 75; main peaks at 410, 440, 540, and 580 nm; 6 W) as well as under pure UV-light irradiation (Philips TL 6W/08; 350 nm; 6 W). The external surface of the catalyst's thin film was exposed to an irradiance of 12.5 and 8 mW/cm^2 under sunlight and pure UV-light respectively. Reaction rates were evaluated under steady state conditions, typically achieved after 4-5 h from the beginning of irradiation. No change in activity was detected for all samples within 24 h after reaching steady state conditions. The concentration of reactants and products was analyzed using an on-line gas chromatograph (Agilent GC 6890) equipped with HP-PLOT-Q/HP-Innowax columns (0.5/0.32 mm I.D. × 30 m) and TCD/FID detectors for the quantification of CO_2 and organic substances (toluene, photo-catalytic products) respectively.

3. Results and discussion

3.1 Catalysts characterization

Figure 1 shows the XRD patterns of the pure and doped TiO_2 samples. Typical spectra of anatase TiO_2 are observed. The main Bragg reflections are indexed in the figure according to the JCPDS card 21-1272 corresponding to the anatase structure. In both TCu*x* and TV*x* series the XRD patterns are consisted with 100 % anatase crystal structure since. No peaks assigned to other oxide phases were found, suggesting that either the dopant metal ions are incorporated in the TiO_2 lattice or Cu and V oxides are very small and dispersed, non-detectable by XRD.[43] The cell parameters of anatase are not affected in the case of Cu due to the low metal doping and the compensation effect related to defect creation, particularly Ti vacancies, vs. the larger Cu ionic radius.[4,47] In the case of V^{4+} the isoelectronic character of V and Ti as well as the similar ionic radius (0.58 Å; compared to Ti^{4+} 0.605 Å) justify the absence of changes in anatase cell parameters. Anatase crystallinity is not affected significantly by the introduction of the metal. The primary crystal size of anatase as estimated by the Scherrer formula using the full width at half maximum (FWHM) of the most intense (1 0 1) diffraction peak is approximately 12 nm. Minimal variations in the anatase crystal size were thus observed within the samples of both series (Table 1).

Table 1 Characteristics of the pure TiO_2,TCu*x* and TV*x* samples.

Sample	Crystal size (nm)	BET ($m^2 g^{-1}$)	Pore volume (ml g^{-1})	Porosity (%)	Pore size (nm)	E_g
TiO_2	11.6	77.6	0.13	33.2	5.7	3.18
TCu0.05	12.5	68.1	0.11	30.5	5.8	3.16
TCu0.1	12.7	70.0	0.11	29.1	5.2	3.15
TCu0.5	12.6	76.5	0.11	30.3	5.5	3.13
TCu1	12.0	81.9	0.12	31.1	5.0	3.09
TV0.05	11.8	73.0	0.11	29.3	5.1	3.16
TV0.1	11.9	75.9	0.11	30.9	5.3	3.14
TV0.5	11.5	74.8	0.11	31.5	5.6	3.09
TV1	11.6	76.0	0.13	33.5	5.9	3.02

Crystal size of anatase determined by XRD using Scherrer equation and the most intense (1 0 1) diffraction peak. Total pore volume taken at relative pressure P/P0 = 0.98. Porosity: estimated based on the density of anatase (3.9 g cm^{-3}) and the pore volume determined using the adsorption branch of the N_2 isotherm at 0.98 relative pressure. Pore size: calculated from the adsorption branch of the N_2 isotherm using the BJH method. E_g was calculated considering the oxides indirect band gap semiconductors.

View Article Online
DOI: 10.1039/C5CY00929D

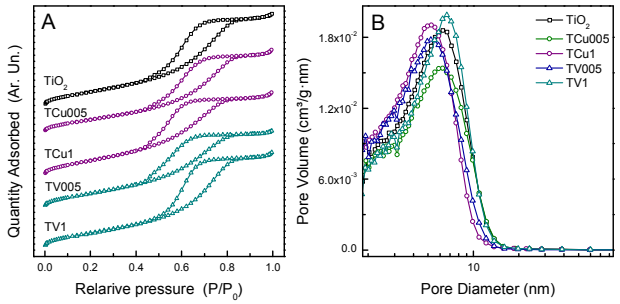

Figure 3. Representative nitrogen adsorption-desorption isotherms (A) and pore size distribution calculated from the adsorption branch of the N_2 isotherm using the BJH method (B) of the pure and metal doped TiO_2 nanomaterials.

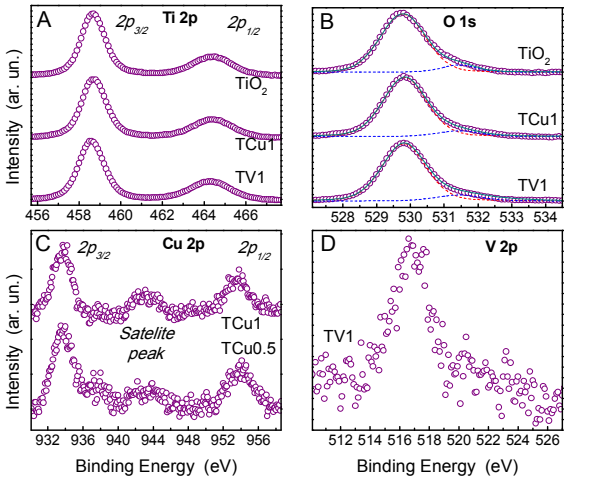

Figure 4. Core level XPS spectra in the Ti 2p (A), O 1s (B), Cu 2p (C) and V 2p (D) region.

The phase composition of the prepared nanomaterials was further studied by Raman spectroscopy. Representative Raman spectra of the undoped and the Cu- and V-doped TiO_2 materials are shown in Figure 2. The exclusive presence of anatase phase is evidenced with peaks at ca. 144, 195, 399, 517 and 639 cm-1, corresponding to the Eg(1), Eg(2), B1g(1), B1g(2), A1g(1) and Eg(3) modes respectively.[18] No crystalline phases of either Cu or V oxide are detected. This is expected for materials with low metal doping levels as those prepared here. The detection of Cu or V oxides would be expected for dopant's concentrations > 1.5 %.[44] Nevertheless, the Raman results are consistent with the XRD.

The BET surface area, total pore volume, porosity and average pore size of the investigated catalysts are listed in Table 1. First to mention is that most of the samples present textural properties in a comparable range. N_2 adsorption-desorption isotherms of the materials are presented in Figure 3A. All samples exhibited typical features of type-IV isotherms with H2 hysteresis loop, attributed to the development of a mesoporous material.[12,45] The surface area is not affected significantly by the presence of the dopant as extracted using the standard BET method.

The adsorption isotherms were used to determine the pore size distribution using the Barret-Joyner-Halender (BJH) method (Figure 3B). The presence of mesoporosity with narrow pore size distributions was observed, implying good homogeneity of the pores. In addition, the average pore diameter is not significantly altered within the samples of both series ranging from 5 to 6 nm.

The surface composition and chemical state were further investigated by means of X-ray photoelectron spectroscopy (XPS). In the XPS survey spectra, peaks due to Ti, O, Cu and V were detected. Figure 4 presents representative XPS spectra of Ti 2p, O 1s, Cu 2p and V 2p core level profiles of the prepared materials. The peaks at approximately 458.6 and 464.3 eV are ascribed to the Ti $2p_{3/2}$ and $2p_{1/2}$ spin-orbit components characteristic of anatase TiO_2 (Figure 4A).[46,47] No obvious differences in the binding energies of the Ti 2p peaks were observed within the samples of both series (i.e. TCu*x* and TV*x*), indicating that the increase of the dopant's concentration does not affect significantly the TiO_2. The O 1s peaks (Figure 4B) were fitted using two symmetric peaks centred at 529.80 and 531.45 eV, attributed to the oxygen lattice ions of the anatase network and surface hydroxyl groups.[47,48]

Figure 4C presents the Cu 2p region of the XPS spectra. Typical Cu 2p XPS spectra are observed. The peaks centred approximately at 933.7 and 953.6 eV, ascribed to the Cu $2p_{3/2}$ and Cu $2p_{1/2}$, accompanied by a satellite peak (clearly observed only for the main Cu $2p_{3/2}$ peak due to the low signal to noise ratio) located at approximately at 941-944.5 eV, indicate the presence of Cu at the (+2) oxidation state.[49,50] The presence of Cu^{1+} is expected at lower binding energies.[49,51] Cu 2p peaks were only detected in the materials with Cu content higher than 0.5 % (Figure 4C). In the TV*x* series, a weak peak at approximately 516.7 eV originating from a single contribution was detected only for the high load sample (TV1) attributed to the V $2p_{3/2}$ at the (+4) oxidation state (Figure 4D).[36]

Light absorption properties were studied by UV–Vis spectroscopy. Starting with the analysis of the band gap (Figure S2A and B), we note firstly that anatase is known to be an indirect band gap semiconductor, although relaxation of energy and momentum rules on the nanoscale may induce direct band gap character.[2,4,52] In any case, the band gap behaviour throughout the series is similar for both cases (e.g. direct and indirect). Table 1 gives the result of the indirect band gap calculation.

Figure 5 displays plots used for band gap estimation as well as the corresponding UV-Vis absorption spectra of the prepared materials (insets). The increase of the absorption at wavelength lower than 390 nm can be assigned to the intrinsic band gap absorption of pure anatase TiO_2. Upon the introduction of the metal, a noticeable shift of the absorption spectra towards the visible-light region can be observed, which increased with increasing dopant's concentration. By extrapolating the linear portion of $(h\nu\alpha)^{1/2}$ versus energy, the band gap (E_g) values were estimated (Table 1). The UV-visible information provides evidence that the dopants induce band gap modification (by altering band structure) even from the lower doping quantity tested here. The trend indicates a

View Article Online
DOI: 10.1039/C5CY00929D
Catal. Sci. Technol. Article

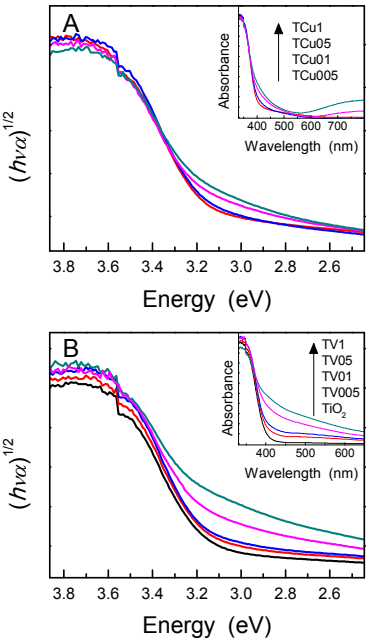

Figure 5. Plot used to estimate band gap considering the oxides indirect semiconductors and diffuse reflectance UV-Vis absorption spectra (insets) of the TCu*x* (A) and the TV*x* nanomaterials (B).

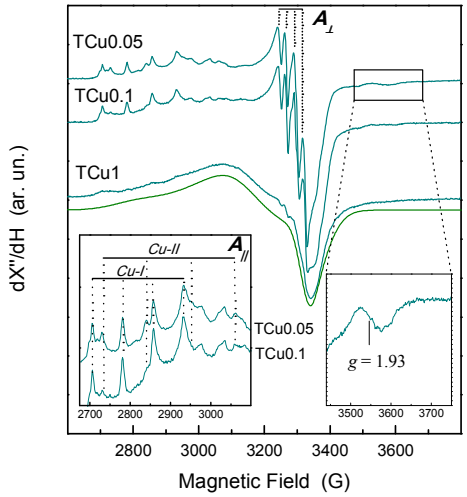

Figure 6. Normalized EPR spectra of the TCu*x* samples taken in dark under vacuum (dashed green spectrum: computer simulation of the broad unstructured Cu^{2+} signal). Left inset: hyperfine splitting in the parallel Cu^{2+} spectral region specifying the two distinct Cu^{2+} species (Cu-I and Cu-II). Right inset: Ti^{3+} centers formed in the TCu0.05 sample. Experimental conditions: 4 G modulation amplitude, 12.4 mW microwave power. For the TCu1 sample a 10-fold smaller receiver gain was used due to signal saturation.

decrease of the band gap energy with increasing dopant concentration in the nanomaterial. In addition, absorption in the visible region is also detected in all but the pure TiO_2 reference sample. In the case of the TCu*x* series, the intensity of the shoulder at ~440 nm and the absorption at ~700-800 nm increases continuously with increasing dopant concentration. The same is observed for the spectra in the TV*x* series in the range 450-700 nm. The light absorption in the visible region can be attributed to the d–d transitions of Cu[25,53] and V,[14,28] similar to that of Fe.[18]

3.2 EPR characterization

3.2.1 Cu^{2+} - doped TiO_2

The EPR spectra of the Cu-doped samples recorded in dark are shown in Figure 6. Two sets of Cu^{2+} EPR signals can be observed. The first dominates the low Cu^{2+} concentration samples presenting well resolved hyperfine splitting and the second, a broad unstructured signal, dominates the high Cu^{2+} loaded samples.

In the low Cu^{2+} doped nanomaterials (samples TCu0.05 and TCu0.1), the EPR signals are characteristic of paramagnetic Cu^{2+} ($3d^9$, S= 1/2) ions in oxygen environment of distorted octahedral geometry. They are characterized by a set of axial or near axial g-values. Hyperfine structure due to I = 3/2 (multiplicity 4) of Cu^{2+} ion can be observed, both in the parallel and perpendicular component of the spectra (low and high magnetic field region of the spectra respectively). Due to the complexity of the experimental spectra, no reasonable computer simulated spectra could be performed. Nevertheless, distinct Cu^{2+} species were detected at the low magnetic field region. Two Cu^{2+} EPR signals can be clearly observed in the parallel region with $g_\parallel^1$=2.435, $A_\parallel^1$=75 G and $g_\parallel^2$=2.370 and $A_\parallel^2$=109 G (named Cu-I and Cu-II respectively, Table 2). They can be attributed to isolated or nearly isolated copper ions and they present similarities in terms of g and A values with Cu^{2+} species previously reported for copper ions incorporated in anatase matrix,[54] as well as for copper-alumina[55,56] and Cu-TiO_2-ZrO_2 ternary samples.[57] The hyperfine spitting of the spectral high field component reveal the presence of at least two Cu^{2+} species with $A_\perp$ = 26 and 18 G having approximately the same g-values ($g_\perp$~2.09). Comparing the relative intensity of signal Cu-I and Cu-II, the Cu-II signal is approximately two times smaller in the TCu0.1 compared to TCu0.05.

Table 2. EPR characteristics of the paramagnetic species in the TCu*x* and the TV*x* series.

Species	$g_\perp$	$g_\parallel$	$A_\perp$	$A_\parallel$	g_{iso}	A_{iso}
Cu-I	~ 2.09	2.434	~ 18	75		
Cu-II	~ 2.09	2.370	~ 26	109		
V-I	1.964	1.914	48	182	1.947	92.7
V-II	1.962	1.919	52	170	1.948	91.3
V-III	1.971	1.928	62	162	1.957	95.3
V-IV					1.93	

The spectral resolution decreases with increasing Cu content. The sample containing 1% of Cu^{2+} is dominated by a broad unstructured signal, extended from 2600 to 3500 G and centered at g~2.1, while a hyperfine structure similar to the low Cu-loaded samples is partially resolved in the perpendicular region. The increase of the line width and the loss of the hyperfine structure can be assigned to the dipole-dipole interaction occurring between neighboring Cu^{2+} sites within CuO clusters formed upon increasing Cu-content. These

View Article Online
DOI: 10.1039/C5CY00929D

are probably nanoclusters of copper ions not detectable with XRD and Raman. This signal accounts for approximately 70 % of the TCu0.5, 20% of the TCu0.1 and less than 3 % of the TCu0.05 spectra.

An additional signal at g = 1.93 is also observed in the TCux series. This signal is not present in the pure anatase TiO_2 reference sample and is attributed to Ti^{3+} centers[23,31] (Figure 6, right inset) previously assigned to surface trapping sites,[23] most likely formed as charge neutrality species due to the incorporation of Cu^{2+} in the TiO_2 lattice. Comparing the normalized EPR spectra of sample TCu0.05 and TCu0.1, the g = 1.93 signal intensity is almost two times smaller in the TCu0.1 and it follows the loss of the Cu-II signal. This may suggest that by increasing the Cu content from 0.05 to 0.1 %, the portion of Cu^{2+} incorporated into the anatase lattice is decreased with respect to the total Cu^{2+} added, resulting to the decrease of the Ti^{3+} EPR signal with respect to the Cu^{2+}. It may also suggest that low Cu loadings favor incorporation of Cu^{2+} into the anatase lattice while for Cu^{2+} > 0.1 % surface Cu-species are also present. Alternatively, it may suggest that charge compensation occurs by different physical phenomena at loadings below/above ca. 0.1 %. Nevertheless, the presence of such signal verified that part of the initial added Cu^{2+} occupied substitutional cation sites in TiO_2 In the normalized spectra in Figure 6, the Ti^{3+} signal is not clearly observed in the high load samples because the spectrum is dominated by the Cu^{2+} signal. The inability to detect Ti^{3+} species with XPS spectroscopy is most likely due to the low Cu-loading (i.e. < 0.1 %) which is overcome with the high sensitivity of EPR. The high sensitivity of EPR is also evidenced on the Cu^{2+} (Figure 6) and V^{4+} (Figure 7, see in the following) EPR signal when compared to the XPS data (Figure 3).

Overall, the present EPR data verify the isolated nature of the cupper species formed in the samples with low metal loading (TCu0.05 and TCu0.1) due to the hyperfine splitting observed in both the parallel and perpendicular component and the formation of Cu clusters upon increasing Cu concentration. In addition, Ti^{3+} centers are formed due to the charge imbalance generated as a consequence of the dopant introduction in the TiO_2 lattice.

3.2.2 V^{4+} - doped TiO_2

Figure 7 presents EPR spectra of the V-TiO_2 samples under vacuum and in dark. In all samples, an eight-component hyperfine structure is observed due to the dipole-dipole interaction of the electronic (S = 1/2) and magnetic moment (I = 7/2, multiplicity 8) of V^{4+} ions (^{51}V, natural abundance of 99.8 %).

Magnetically isolated species, characterized by axial g and A tensors, have been detected. The TV0.05 and TV0.1 spectra present basically the same profile and can be analyzed as a superposition of two different V^{4+} species, with slightly different principle values (Table 2), suggesting minor differences in the coordination environment (specie V-I and V-II). V^{4+} presenting similar g and A tensors have been previously attributed to V^{4+} centers located within the anatase bulk.[58] In

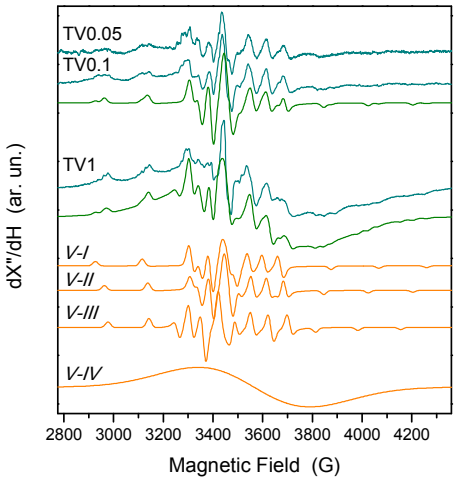

Figure 7. Normalized EPR spectra of the TVx samples in dark under vacuum. Spectra specification: Blue - experimental spectra; Green - total simulated spectra; Orange - individual simulated spectra (V-I to V-IV). Experimental conditions: 10 G modulation amplitude, 4.9 mW microwave power.

the TV0.05 sample, the hyperfine structure in the parallel region cannot be clearly resolved due to the low signal intensity.

At higher vanadium concentrations, the interaction between different V^{4+} ions increases giving rise to a dipolar broadening (see spectrum TV1). This results to an additional broad, unstructured, singlet EPR spectrum centered at g = 1.93 with linewidth of approximately 400 G (specie V-IV). Similar EPR signals have been previously reported for V-doped TiO_2 anatase samples.[59-61] Nevertheless, hyperfine splitting due to isolated V^{4+} species can still be detected. In addition to the two V^{4+} spectra detected in the low V-loaded samples (TV0.05 and TV0.1), a new V^{4+} spectrum with g and A principle components $g_{\perp}$ = 1.971, $g_{||}$ = 1.928, $A_{\perp}$ = 62 G and $A_{||}$ = 162 G was detected (specie V-III). The contribution of the broad singlet EPR signal is approximately 85 % for the TV1 sample and 39 % for the TV0.5 (based on double integration analysis of the simulated spectra), attributed to magnetically interacting vanadium species, indicating the formation of oxide. As in the case of the TCux nanomaterials, these are nanoclusters not detectable with XRD and Raman.

Based on the analysis of the g_{iso} and A_{iso} values[62] of the three isolated V^{4+} spectra, the two species (V-I and V-II) detected at low V^{4+} doping do not present pronounced vanadyl character compared to the third specie (V-III) detected only for V^{4+}> 0.5 %. This indicates that the third specie might be located on the surface of the material as surface vanadyl sites. Of importance is to mention that, in contrast to the Cu-doped samples, no EPR signal attributed to Ti^{3+} was detected for the V-doped materials which can be attributed to the absence of charge imbalance due to the isolectronic properties of Ti^{4+} and V^{4+}.

At this point we highlight the fact that while no difference was observed within the samples containing different amount of dopant with XRD and Raman and only the nanomaterials

View Article Online
DOI: 10.1039/C5CY00929D

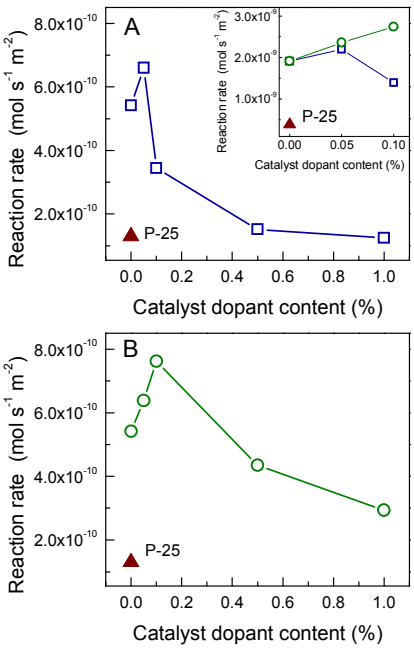

Figure 8. Surface-area-normalized steady state reaction rates for toluene photo-oxidation under sunlight irradiation by the Cu-doped (A) and V-doped (B) nanomaterials. Inset: photocatalytic results under pure UV-light irradiation for selected samples (TCu*x*: squares, TV*x*: cycles, triangle: P-25).

with relatively high dopant content could be studied with XPS, EPR provided structural information for both the low and high doped catalysts in the two series.

The structural and electronic effects of Cu and V doping on the anatase can be thus summarized as being related to the introduction of the dopant in anatase matrix, the formation of isolated species and clusters at low and high dopant concentration respectively, altering the band gap energy and in some cases introducing Ti^{3+} centers in the crystal structure. The dopants introduced do not appear to substantially modify primary particle size, the crystal structure as well the texture properties of the nanomaterials.

3.3 Photocatalytic activity

Figure 8 shows steady state reaction rates for the gas-phase photo-oxidation of toluene by the two TiO_2 series under artificial sunlight and pure UV irradiation (inset), taking into account the different BET surface area of the samples. Expressing the rate per weight unit (mol s^{-1} g^{-1}) gives essentially a similar general behavior as the one presented in Figure 8, since the specific surface area is not significantly altered especially for low dopant's content (Table 1). For comparison, the photocatalytic results obtained for the commercial reference TiO_2 Degussa P-25 is also included in the figure. Catalytic tests carried out without photocatalysts or irradiation confirmed that the measured activities were fully attributed to photo-induced processes on TiO_2. CO_2 and benzaldehyde were the only gaseous products detected during toluene photo-oxidation. No significant differences were detected on the selectivity towards CO_2 or benzaldehyde within the samples of both series. The time evolution of toluene for representative examples is presented in Figure S2 of the supporting information.

A first important observation is that most of the prepared nanomaterials improve the performance of P-25. In particular, the most active doped TiO_2 nanomaterial (TV0.1) presents a six-fold higher photoactivity compared to pristine P-25. In addition, a number of the doped-TiO_2 nanostructures are more active than the pure TiO_2 nanomaterial having a similar particle size and obtained using the same preparation procedure.

In the TCu*x* series (Figure 8A), the photoactivity under solar light irradiation is continuously decreased with increasing Cu-content. Compared to the pure TiO_2 reference sample, photoactivity is higher only for the low-doped sample (TCu0.05). In the TV*x* series (Figure 8B) photoactivity is increased for the two low V-doped nanomaterials presenting higher efficiency than the pure TiO_2 reference sample and it is decreased at higher dopant concentration. Therefore, toluene photo-excitation appears to be favored at low metal doping and seems clearly detrimental for high levels. This suggests the presence of a turning point where a beneficial/detrimental effect on photoactivity is detected with respect to the reference pure TiO_2 sample in both TCu*x* and TV*x* series where the dopant content varies. This turning point is observed at relatively higher dopant amount in the TV*x* series (i.e. TV0.5) compared to the TCu*x* nanomaterials (i.e. TCu0.1). Nevertheless, in both cases it is observed at low dopant concentration, it is approximately at similar levels as previously reported[7,14] and it falls within the optimal area defined by Bloh *et al*..[63]

The inset in Figure 8 shows results for selected samples in similar conditions to those reported in Figure 8 but using pure UV light excitation. A similar trend of the photoactivity with respect to the dopant level is observed irrespective of the light source nature. However, smaller differences were detected within the samples tested under pure UV light irradiation, since the improvement of photocatalytic activity is more pronounced under solar light irradiation. This indicates that visible light activity is induced in the doped nanomaterials. However, although electronic properties linked with the light absorption properties of the nanomaterials might have an impact, is not the dominant parameter determining photoactivity.

Regarding photocatalytic activity, one should mention that it is a result of different factors, including crystalline phases present in the nanomaterial, particle size, specific surface area, porosity, band gap, composition, charge separation and many others. Herein, precise control of the synthesis process and the mild conditions applied for the nanomaterials modification, resulted to practically unchanged nanostructures regarding crystal structure, crystallinity and texture properties, minimizing the differences within samples of the two series. As was stated above, pure electronic properties are not of significance in interpreting fully photoactivity. Therefore, additional EPR experiments were contacted to study the

View Article Online
DOI: 10.1039/C5CY00929D

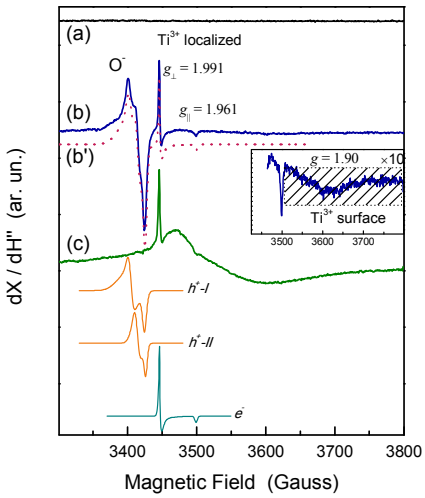

Figure 9. EPR spectra of (a) the pure TiO_2 sample in dark, (b) after 20 min UV irradiation with the corresponding simulated spectrum (b′, sum of the three individual signals), (c) after 20 min UV irradiation in the presence of iso-propanol. The individual simulated spectra (h^+-I, h^+-II and e^-) are given at the bottom of the figure. Experimental conditions: 2 G modulation amplitude, 4.9 mW microwave power.

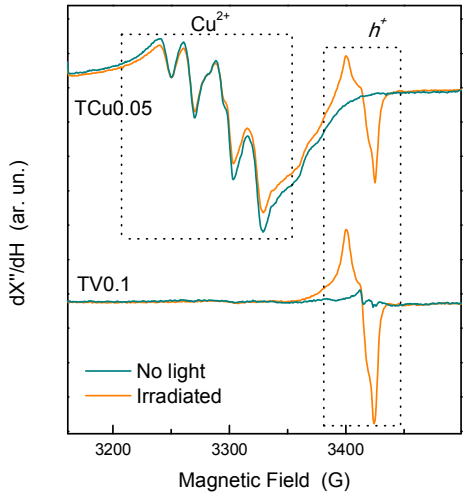

Figure 10. EPR spectra of the TCu0.05 (upper) and TV0.1 nanomaterial (lower) taken in dark (blue) and under 20 min UV irradiation (orange). Experimental conditions: same as in Figure 9.

Table 3. *g*-values of the photogenerated species observed in the nanomaterials prepared. Error: ± 0.0002.

Sample	H-I (O^-)			H-II (O^-)		Ti-I (Ti^{3+})	
	g_1	g_2	g_3	$g_\perp$	$g_{\|\|}$	$g_\perp$	$g_{\|\|}$
TiO_2	2.0182	2.0145	2.0040	2.0102	2.0020	1.991	1.961
TCu005	2.0185	2.0142	2.0040	2.0105	2.0022	–	–
TCu01	2.0187	2.0145	2.0040	2.0105	2.0022	–	–
TCu05	–	–	–	–	–	–	–
TCu1	–	–	–	–	–	–	–
TV005	2.0185	2.0142	2.0040	2.0105	2.0022	–	–
TV01	2.0185	2.0142	2.0040	2.0105	2.0022	–	–
TV05	2.0184	2.0142	2.0040	2.0105	2.0022	–	–
TV1	2.0180	2.0140	2.0032	2.0105	2.0022	–	–

charge carriers formation and abundance under light irradiation.

3.4 Charge trapping sites on TiO_2

Figure 9 presents EPR spectra of the pure TiO_2 anatase reference sample in dark (a) and under light irradiation (b and c). No EPR signal is detected in the spectra recorded in dark (Figure 9a). After 20 min UV irradiation at liquid N_2 temperature, two sets of EPR signals are detected (Figure 9b). The low field feature is assigned to oxygen species, holes (h^+) trapped at oxygen anions (O^-). As summarized in Table 3, computer simulation of the experimental data allowed the determination of two overlapping signals (h^+-I and h^+-II) attributed to h^+ trapped at two different O^- sites.[24,62] The *g*-values of both signals are similar to h^+ species previously observed in TiO_2 anatase prepared and treated in a similar way as those here.[21,22,64-72]

The high field component of the spectrum contains a sharp EPR feature of axial symmetry, $g_\perp = 1.991$ and $g_{||} = 1.961$ (Ti-I). Based on the EPR characteristics in terms of *g*-values and spectral shape, this signal can be assigned to electrons trapped at localized states in the anatase structure as Ti^{3+} centers.[68,69,71-73] These species have been previously attributed to centers located in the inner part of the particle.[22,68,72-74] The intensity of the Ti^{3+} signal is not affected by the presence of atmospheric O_2 which further confirmed their location in the lattice of anatase (data not shown). It should be noted that Ti^{3+} centers formed in the bulk of the material act as recombination centers, reducing the activity of the surface reactions.[71,72] These centers are different from Ti^{3+} centers that give rise to a broad signal at higher field (the negative contribution of which can be observed in the inset in Figure 9 at $g \sim 1.90$) and have been previously attributed to centers at disordered environment at the crystals surface.[73,74] Double integration of the single spectra corresponding to h^+ (h^+-I and h^+-II) and e^- (Ti-I) trapped at localized states reveals that e^- are less than 10 % of the trapped h^+. The signal intensity of the trapped charges remains essentially constant at T = 77 K and in the dark during the course of the experiment. After subsequent warming of the sample at room temperature, both h^+ and e^- EPR signals are lost (data not shown) as a result of the h^+/e^- recombination process.

In the presence of isopropanol, a well known hole scavenger, the EPR signal assigned to trapped holes disappears completely (Figure 9c). The sharp Ti-I signal with $g_\perp = 1.991$, $g_{||} = 1.961$ remains essentially unchanged and a new signal at $g \sim 1.95$ assigned to different Ti^{3+} centers appears.[31,65] This second species is located at the surface of the solid and is extended over 320 G due to the relatively disordered environment.[74,75] These observations are in accordance with previous reports[31,71] and clearly demonstrate that the holes are trapped at the surface since they easily react with hole scavengers such as isopropanol. Therefore, they are consumed during photo-oxidation of toluene.

Overall, based on the above observations and in accordance with the well established charge transfer processes

View Article Online
DOI: 10.1039/C5CY00929D

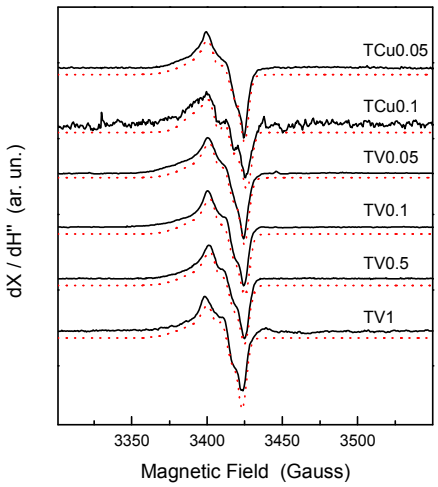

Figure 11. Normalized EPR spectra of metal doped TiO_2 taken after 20 min UV irradiation in vacuum after subtracting a proper amount of the corresponding spectra recorded in dark. Dashed red lines: computer simulated spectra using two overlapping h^+ signals. Experimental conditions: same as in Figure 9.

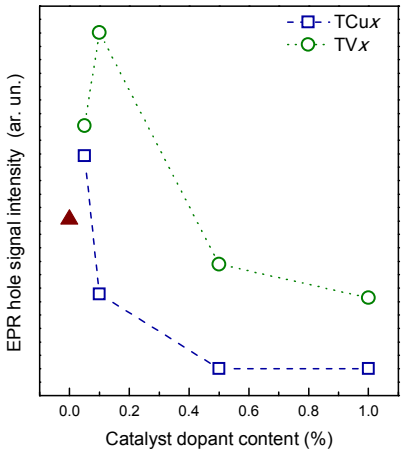

Figure 12. Relative EPR intensity of the hole signal in the pure (solid symbol) and the TC*ux* (blue color) and TV*x* (green color) series.

in similar systems,[1,68,69] we indicate the following charge transfer steps under light irradiation:

$$TiO_2 + h\nu \rightarrow e^- + h^+ \quad (1)$$
$$e^- + Ti^{4+} \rightarrow Ti^{3+} \quad (2)$$
$$h^+ + O^{2-} \rightarrow O^- \quad (3)$$

indicating the charge carriers formation under irradiation (1) and the electron (2) and hole (3) trapping at localized states.

Changes in the EPR spectra were also detected for the doped materials under irradiation. Representative spectra of the catalysts taken in the dark and under irradiation are presented in Figure 10. Figure 11 presents EPR spectra of the doped materials in the region of the trapped h^+ and e^- normalized to their second integral. The spectra were taken under irradiation and in vacuum and are presented after removing a proper amount of the corresponding spectra recorded in dark. Two important information can be extracted when compare the pure with the doped materials: i) an EPR feature identical to the one of the pure TiO_2 reference sample assigned to trapped holes is observed in the majority of the doped TiO_2 materials. No hole signal was detected for the TCu0.5 and TCu1 samples. The experimental spectra were simulated (red spectra in Figure 11) by assuming two overlapping signals similar to those used for the pure TiO_2 reference; ii) the Ti^{3+} EPR signal of the e^- trapped at localized centers (Ti-I) detected in the undoped TiO_2 reference sample disappears completely in the presence of the dopant in both TC*ux* and the TV*x* series (Figure 11). These results clearly indicate that in the metal doped anatase nanomaterials photoinitiated charge formation takes place, forming identical h^+ species as those in the pure reference TiO_2 catalyst.

Regarding the O^- signal, clear differences in the intensity of the hole signal were observed by varying the amount of the dopant. The relative signal intensity corresponding to trapped holes as O^- centers versus the dopant's concentration is presented in Figure 12. The amount of trapped holes which ultimately drives the surface photooxidation processes follows a belt-like shape with optimum conditions achieved at low or moderate dopant concentration. In the case of the Cu^{2+}-doped materials, the intensity of the hole signal when compared to the pure TiO_2 reference is higher only for the TCu0.05 sample and it is not detected in the high-loaded samples (Figure 12, samples TCu0.5 and TCu1). In the case of the TV*x* series, the O^- signal intensity is higher in the TV0.05 and TV0.1 compared to the pure TiO_2 sample and deteriorates at higher V^{4+} concentrations. This loss in both series for dopant content higher than 0.5 % cannot be attributed to shading/shielding effect taking into account the low dopant to Ti surface ratio based on XPS. The relative contribution of the two individual hole signals (h^+-I and h^+-II), calculated as the % of the total intensity of the hole signal (I + II), is essentially stable in all samples and is not affected by the dopant concentration. At this point, we highlight the clear resemblance of the EPR h^+ signal intensity variation with the catalytic activity presented in Figure 8 for both series. It has been shown previously in V-doped TiO_2 that the photocatalytic degradation of dyes in solution follows the hydroxyl radical formation,[43] which in turn is related to h^+ production.

The absence of the Ti-I EPR signal assigned to localized sites of trapped electrons (i.e. Ti^{3+}) in all doped nanomaterials under irradiation can be exclusively assigned to the presence of the dopant. This is based on the general mechanism of charge photo-generation and transfer process described in reactions (1)-(3)[1,68,69] and is further supported by the holes formation in the doped materials (detected as O^- centers) as well as the detection of Ti^{3+} centers as localized electron trapping sites in the pure TiO_2 material. In such a scheme, the straightforward explanation would be the presence of an effective electron transfer process where the dopant plays the role of the acceptor for the photogenerated electrons,[31,38,73] minimizing the Ti^{3+} signal at $g_\perp = 1.991$ (i.e. Ti-I specie). In fact, a decrease of the Cu^{2+} EPR signal intensity was detected in the TCu0.05 nanomaterial upon light irradiation (Figure 10, marked area). This suggests reduction of Cu^{2+} to the EPR silent Cu^+ via accepting photogenerated e^-.[31,38] The signal intensity was

View Article Online
DOI: 10.1039/C5CY00929D

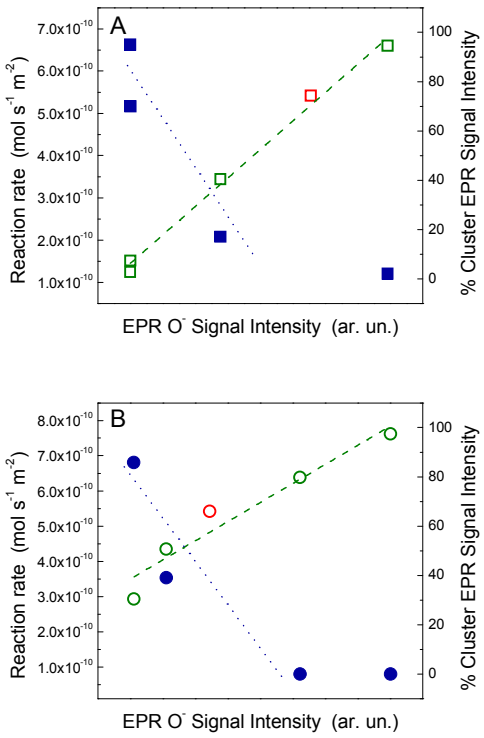

Figure 13. Correlation plots between the EPR hole signal intensity and the steady state reaction rates of toluene photodegradation (open symbols, left Y-axis) and the EPR hole signal intensity with the cluster formation (solid symbols, right Y-axis) for the TCu*x* (A) and the TV*x* (B) series. The pure TiO_2 reference sample is indicated with the red symbol. Lines are guide for the aids.

restored after exposing the sample to ambient atmosphere. No such difference was detected for the V-doped materials. However, the vanadium case is more complicated due to the possible participation of three different oxidation states (+5, +4, +3). This electron transfer process is expected to have an impact on the photoactivity, via eliminating the Ti-I specie formed in the bulk of the material[22,68,72,73] and facilitating charge separation.

Figure 13 shows correlation plots between the EPR hole signal intensity versus the steady state reaction rates for the gas-phase toluene photodegradation (left Y-axis) and the cluster formation (right Y-axis) for the TCu*x* (Figure 13A) and TV*x* series (Figure 13B). A linear relation is observed in both cases. A linear trend between catalytic activity as well as the metal cluster formation is observed as a function of hole formation in both cases. In the second case, note that some samples do not have a cluster contribution to the doping metal distribution and generates two linear response regions (one trivial, with null slope). Given that holes are the primary photogenerated species responsible for toluene degradation by TiO_2,[5,6,73] the difference in photoactivity detected between samples in both series (Figure 8) is due to the relative abundance of such species in the nanomaterial, as expressed in Figure 12 and indicated by the correlation plots in Figure 13. On the other hand, the trend of cluster formation as expressed by the broad unstructured signal in the EPR spectra of both Cu and V series (Figure 6 and 7 respectively) is inversely proportional to the EPR hole signal intensity.

The interpretation of such correlation plots would imply that photocatalytic degradation of toluene is directly correlated with the hole formation, which in turn is tuned by the dopant's species in the nanomaterial. Isolated and highly dispersed Cu^{2+} and V^{4+} species are beneficial for toluene photodegradation while the presence of metal oxide clusters reduces photoactivity via deteriorating hole formation. This mechanism is controlled by the dopant's content in the nanostructures and in our materials the turning points are 0.1 % and 0.5 % for Cu-doped and V-doped anatase TiO_2 respectively. The isolated dopant's species restrain the recombination rate of electron and hole pairs by accepting photogenerated electrons demonstrated by the absence of Ti^{3+} centers as localized electron traps in the doped materials (Figure 8 and 9). Once efficiently separated, the photogenerated charges can be more effectively involved in oxidation and reduction reactions enhancing toluene's photodegradation. On the other hand, by increasing the dopant's content above a certain point in the final nanomaterial, metal clusters are formed acting as recombination centers[38,63] of photogenerated e^- and h^+ suppressing photoactivity. Despite the difference in the actual metal content linked with the turning point of the catalytic activity (0.1% for Cu^{2+} and 0.5% for V^{4+}), the data presented herein verify that photoactivity is governed by the same mechanism in both TiO_2 series, suggesting that this interpretation may find application in similar systems.

Conclusions

Two series of Cu^{2+} and V^{4+} doped TiO_2 anatase samples were prepared via the microemulsion synthetic route. The electronic and structural properties of the metal containing titania nanomaterials were fully characterized. Nanomaterials with primary particle size and texture properties in a comparable range were developed while band gap narrowing was observed for the doped nanostructures. EPR spectroscopy revealed the presence of different dopant species via varying their nominal concentration and their effect on the abundance and stability of photogenerated charge carriers, e^- and h^+ pairs. Complete structural and electronic characterization combined with catalytic results of toluene photo-oxidation under both pure UV and artificial solar light irradiation allowed the determination of the factors affecting photoactivity. EPR provided direct experimental evidence that photoinitiated charge formation took place in the nanomaterials. Different dopant species were identified. Isolated and highly dispersed Cu^{2+} and V^{4+} species favored hole formation while at the same time decrease the amount of Ti^{3+} centers (i.e. trapped e^- at localized states) under irradiation. It is proposed that the presence of such dopant species is responsible for the enhanced photocatalytic activity via increasing the charge separation efficiency acting as efficient electron scavengers and increasing the surface availability of the key charge carrier,

View Article Online
DOI: 10.1039/C5CY00929D
Catal. Sci. Technol. Article

the holes. At higher dopant levels, metal clusters were formed acting as recombination centers deteriorating photoactivity.

Acknowledgements

Financial support by project MINECIO_Spain ENE2013-46624-C4-1-R (partially supported by FEDER) is fully acknowledged. K.C.C. acknowledges the TALENTS FVG Programme for a Post-doctoral fellowship funded from the European Social Fund (Operational Programme 2007-2013, Objective 2 Regional Competitiveness and Employment, Axis 5 Transnational cooperation, TALENTS FVG Programme).

References

1 A. Kubacka, M. Fernandez-Garcia and G. Colon, *Chem. Rev.*, 2012, **112**, 1555.
2 L. Jim, W. Zhou, G. Tian and H. Fu, *Chem. Soc. Rev.*, 2013, **42**, 9509.
3 Z. Wang, Y. Liu, B. Huan, Y. Dai, Z. Lou, G. Wang, X. Zhang and X. Quin, *Phys. Chem. Chem. Phys.*, 2014, **16**, 2758.
4 M. Fernández-García, A. Martínez-Arias, J.C. Hanson and J.A. Rodriguez, *Chem. Rev.*, 2004, **104**, 4063.
5 M.J. Munoz-Batista, M.N. Gomez-Cerezo, A. Kubacka, D. Tudela and M. Fernández-García, *ACS Catal.*, 2014, **4**, 63.
6 M.J. Munoz-Batista, A. Kubacka and M. Fernández-García, *ACS Catal.*, 2014, **4**, 4277.
7 S.G. Ghugal, S.S. Umar and R. Sasikala, *Mater. Res. Bull.* 2014, **61**, 298.
8 C.W. Lai and S. Sreekantan, *Int. J. Hydrogen Energ.*, 2013, **38**, 2156.
9 D. Yang, J. Zhao, H. Liu, Z. Zheng, M.O. Adebajo, H. Wang, X. Liu, H. Zhang, J.-C. Zhao, J. Bell and H. Zhu, *Chem. Eur. J.* 2013, **19**, 5113.
10 D.J. Yang, H.W. Liu, Z.F. Zheng, Y. Yuan, J.C. Zhao, E.R. Waclawik, X.B. Ke and H.Y. Zhu, *J. Am. Chem. Soc.*, 2009, **131**, 17885.
11 K. Bhattarcharyya, J. Majeed, K.K. Dey, P. Ayyub, A.K. Tyagi and S.R. Bharadwajd, *J. Phys. Chem. C*, 2014, **148**, 15946.
12 K.C. Christoforidis, S.J.A. Figueroa and M. Fernandez-Garcia, *Appl. Catal. B Environm.*, 2012, **117-118**, 310.
13 A. Kubacka, G. Colón and M. Fernández- García, *Catal. Today*, 2009, **143**, 286.
14 B. Tian, C. Li, F. Gua, H. Jianga, Y. Hu and J. Zhang, *Chem. Eng. J.*, 2009, **151**, 220.
15 A. Kubacka, B. Bachiller-Baeza, G. Colón and M. Fernández-García, *Appl. Catal. B Environm.*, 2010, **93**, 274.
16 A. Kubacka, G. Colón and M. Fernández-García, *Appl. Catal. B Environm.*, 2010, **95**, 238.
17 M.J. Muñoz-Batista, A. Kubacka, M.N. Gómez-Cerezo, D. Tudela and M. Fernández-García, *Appl. Catal. B Environm.,* 2013, **140-141**, 626.
18 K.C. Christoforidis, A. Iglesias-Juez, S.J.A. Figueroa, M. Di Michiel, M.A. Newton and M. Fernandez-Garcia, *Catal. Sci. Technol.*, 2013, **3**, 626.
19 S. Ikeda, N. Sugiyama, B. Pal, G. Marci, L. Palmisano, H. Noguchi, K. Uosaki and B. Ohtani, *Phys. Chem. Chem. Phys.*, 2001, **3**, 267.
20 M.K. Kahn, J. Xu, W. Cao and Z.-K. Liu, *J. Nanosci. Nanotechnol.*, 2014, **14**, 6865.
21 T. Berger, O. Diwald, E. Knozinger, M. Sterrer and J.T. Yates Jr, *Phys. Chem. Chem. Phys.*, 2006, **8**, 1822.
22 S.-C. Ke, T.-C. Wang, M.-S. Wong and N.O. Gopal, *J. Phys. Chem. B*, 2006, **110**, 11628.
23 D.C. Hurum, K.A. Gray, T. Rajh and M.C. Thurnauer, *J. Phys. Chem. B*, 2005, **109**, 977.
24 R. Scotti, I.R. Bellobono, C. Canevali, C. Cannas, M. Catti, M. D'Arienzo, A. Musinu, S. Polizzi, M. Sommariva, A. Testino and F. Morazzoni, *Chem. Mater.*, 2008, **20**, 4051.
25 H. Yu, H. Irie and K. Hashimoto, *J. Am. Chem. Soc.*, 2010, **132**, 6898.
26 S. Klosek and D. Raftry, *J. Phys. Chem. B*, 2001, **105**, 2815.
27 M. Anpo and M. Takeuchi, *J. Catal.* 2003, **216**, 505.
28 A. Kubacka, A. Fuerte, A. Martínez-Arias and M. Fernández-García, *Appl. Catal. B Environm.*, 2007, **74**, 26.
29 H. Huang, S. Way, Y. Zhang and P.K. Chu, *RSC Adv.*, 2014, **4**, 14219.
30 P. Devaraji, N.K. Sathu and C.S. Gopinath, *ACS Catal.*, 2014, **4**, 2844.
31 Y. Nosaka, S. Takahashi, H. Sakamoto and A.Y. Nosaka, *J. Phys. Chem. C*, 2011, **115**, 21283.
32 A. Di Paola, G. Marci, L. Palmisano, M. Schiavello, K. Uosaki, S. Ikeda and B. Ohtani, *J. Phys. Chem. B*, 2002, **106**, 637.
33 K. Nagaveni, M.S. Hegde and G. Madras, *J. Phys. Chem. B*, 2004, **108**, 20204.
34 J. Zhonga, J. Xub and Q. Wang, *Appl. Sur. Sci.*, 2014, **315**, 131.
35 P.V.R.K. Ramacharyulu, J. Praveen Kumar, G.K. Prasad, B. Singh, B. Sreedhar and K. Dwivedi, *J. Mol. Catal. A: Chem.*, 2014, **387**, 38.
36 H. Liu, Y. Wu and J. Zhang, *ACS Appl. Mater. Interfaces*, 2011, **3**, 1757.
37 K. Bhattacharyya, S. Varma, A.K. Tripathi, S.R. Bharadwaj and A.K. Tyagi, *J. Phys. Chem. C*, 2008, **112**, 19102.
38 G. Li, N.M. Dimitrijevic, L. Chen, T. Rajh and K.A. Gray, *J. Phys. Chem. C*, 2008, **112**, 19040.
39 Z. Luo, A.S. Poyraz, C-H. Kuo, R. Miao, Y. Meng, S-Y. Chen, T. Jiang, C. Wenos, and S.L. Suib, *Chem. Mater.*, 2015, **27**, 6.
40 H. Chen and Y. Xu, *J. Phys. Chem. C*, 2012, **116**, 24582.
41 S. Stoll and A. Schweiger, *J. Magn. Reson.*, 2006, **178**, 42.
42 A. Fuerte, M.D. Hernández-Alonso, A.J. Maira, A. Martínez-Arias, M. Fernández-García, J.C. Conesa, J. Soria and G. Munuera, *J. Catal.*, 2002, **212**, 1.
43 S.M. Chang and W.S. Liu, *Appl. Catal. B Environm.*, 2011, **101**, 333.
44 P.G.W.A. Kompio, A. Brockner, F. Hipler, G. Auer, E. Loffler and W. Gronert, *J. Catal.*, 2012, **286**, 237.
45 P.Z. Araujo, V. Luca, P.B. Bozzano, H.L. Bianchi, G.J.A.A. Soler-Illia and M.A. Blesa, *ACS Appl. Mater. Interfaces*, 2010, **2**, 1663.
46 C.D. Wagner, W.M. Riggs, L.E. Davis and J.F. Moulder, Handbook of X-ray Photoemission Spectra; G.E. Muilenberg, Ed.; Perkin-Elmer: Eden Prairie, MN, 1976.
47 A. Kubacka, M. Fernández-García and G. Colón, *J. Catal.*, 2008, **254**, 272.
48 G. Colon, M.C. Hidalgo, G. Munuera, I. Ferino, M.G. Cutrufello and J.A. Navio, *Appl. Catal. B Environm.*, 2006, **63**, 45.
49 K.V.R. Chary, G.V. Sagar, D. Naresh, K.K. Seela and B. Sridhar, *J. Phys. Chem. B*, 2005, **109**, 9437.
50 S.N.R. Inturi, T. Boningari, M. Suidan and P.G. Smirniotis, *Appl. Catal. B Environm.*, 2014, **144**, 333.
51 K. Lalitha, G. Sadanandam, V.D. Kumari, M. Subrahmanyam, B. Sreedhar and N.Y. Hebalkar, *J. Phys. Chem. C*, 2010, **114**, 22181.
52 N. Serpone, D. Lawless and R. Khairutdinov, *J. Phys. Chem.*, 1995, **99**, 16555.
53 M. Liu, X. Qiu, M. Miyauchi and K. Hashimoto, *Chem. Mater.*, 2011, **23**, 5282.
54 C. Pruvost, D. Courcot, E. AbiAad, E.A. Zhilinskaya and A. Aboukais, *J. Chim. Phys.*, 1999, **96**, 1527.
55 G. Centi, S. Perathoner, D. Billing and E. Giamello, *J. Catal.*, 1995, **151**, 75.

View Article Online
DOI: 10.1039/C5CY00929D

56 W. Dow, Y. Wang and T.J. Huang, *J. Catal.*, 1996, **160**, 155.
57 K.V.R. Chary, G.V. Sagar, D. Naresh, K.K. Seela and B. Sridhar, *J. Phys. Chem. B*, 2005, **109**, 9437.
58 J.P. Balikdjian, A. Davidson, S. Launay, H. Eckert and M. Che, *J. Phys. Chem. B*, 2000, **104**, 8931.
59 S. Klosek and D. Raftery, *J. Phys. Chem. B*, 2001, **105**, 2815.
60 J.P. Balikdjian, A. Davidson, S. Launay, H. Eckert and M. Che, *J. Phys. Chem. B*, 2000, **104**, 8931.
61 M.C. Paganini, L. Dall'Acqua, E. Giamello, L. Lietti, P. Forzatti and G. Busca, *J. Catal.*, 1997, **166**, 195.
62 A. Davidson and M. Che, *J. Phys. Chem.*, 1992, **96**, 9909.
63 J.Z. Bloh, R. Dillert and D.W. Bahnemann, *J. Phys. Chem. C*, 2012, **116**, 25558.
64 M. D'Arienzo, J. Carbajo, A. Bahamonde, M. Crippa, S. Polizzi, R. Scotti, L. Wahba and F. Morazzoni, *J. Am. Chem. Soc.*, 2011, **133**, 17652.
65 O.I. Micic, Y. Zhang, K.R. Cromack, A.D. Trifunac and M.C. Thurnauer, *J. Phys. Chem.*, 1993, **97**, 7277.
66 J.M. Coronado, A.J. Maira, J.C. Conesa, K.L. Yeung, V. Augugliaro and J. Soria, *Langmuir*, 2001, **17**, 5368.
67 J.M. Coronado and J. Soria, *Catal. Today*, 2007, **123**, 37.
68 T. Berger, M. Sterrer, O. Diwald and E. Knozinger, *ChemPhysChem*, 2005, **6**, 2104.
69 T. Berger, M. Sterrer, O. Diwald, E. Knozinger, D. Panayotov, T. L. Thompson and J.T. Yates Jr., *J. Phys. Chem. B*, 2005, **109**, 6061.
70 T. Berger, M. Sterrer, S. Stankic, J. Bernardi, O. Diwald and E. Knozinger, *Mater. Sci. Eng. C*, 2005, **25**, 664.
71 Y. Nakaoka and Y. Nosaka, *J. Photochem. Photobiol. A Chem.*, 1997, **110**, 299.
72 C. Praveen Kumar, N. Obularajugari Gopal, T. Chung Wang, M.-S. Wong and S. Chu Ke, *J. Phys. Chem. B*, 2006, **110**, 5223.
73 G. Barolo, S. Livraghi, M. Chiesa, M.C. Paganini and E. Giamello, *J. Phys. Chem. C*, 2012, **116**, 20887.
74 J. Biedrzycki, S. Livraghi, E. Giamello, S. Agnoli and G. Granozzi, *J. Phys. Chem. C*, 2014, **118**, 8462.
75 S. Livraghi, M. Chiesa, M.C. Paganini and E. Giamello, *J. Phys. Chem. C*, 2011, **115**, 25413.

View Article Online
DOI: 10.1039/C5CY00929D

Graphical abstract

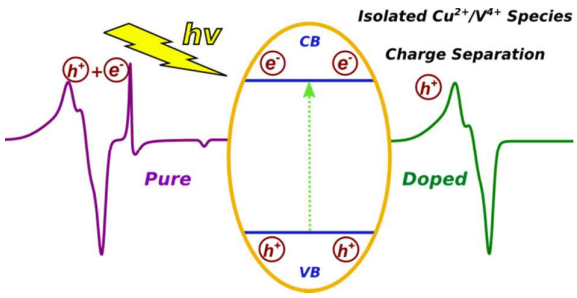

Isolated dopant's species and metal-cluster formation regulate photoactivity and charge carriers formation via accepting e^- and eliminating Ti^{3+} states.